Frontiers of Information Technology & Electronic Engineering
www.jzus.zju.edu.cn; engineering.cae.cn; www.springerlink.com
ISSN 2095-9184 (print); ISSN 2095-9230 (online)
E-mail: jzus@zju.edu.cn

Review:

Heterogeneous III-V silicon photonic integration: components and characterization*

Shang-jian ZHANG[†1], Yong LIU[†‡1], Rong-guo LU[1], Bao SUN[1], Lian-shan YAN[2]

[1]*School of Optoelectronic Science and Engineering, University of Electronic Science and Technology of China, Chengdu 610054, China*

[2]*Center for Information Photonics and Communications, School of Information Science and Technology, Southwest Jiaotong University, Chengdu 610031, China*

[†]E-mail: sjzhang@uestc.edu.cn; yongliu@uestc.edu.cn

Received Aug. 11, 2018; Revision accepted Dec. 2, 2018; Crosschecked Apr. 11, 2019

Abstract: Heterogeneous III-V silicon (Si) photonic integration is considered one of the key methods for realizing power- and cost-effective optical interconnections, which are highly desired for future high-performance computers and datacenters. We review the recent progress in heterogeneous III-V/Si photonic integration, including transceiving devices and components. We also describe the progress in the on-wafer characterization of photonic integration circuits, especially on the heterogeneous III-V/Si platform.

Key words: Heterogeneous photonic integration; Optical interconnection; On-wafer characterization
https://doi.org/10.1631/FITEE.1800482 **CLC number:** O439

1 Introduction

High-density and cost-effective photonic integration circuits (PICs) are considered the promising candidates for future high-performance computers and datacenters (Arakawa et al., 2013). High-level silicon photon integration technologies have been demonstrated with scalability up to a large substrate level (450 mm today) and have compatibility with complementary metal-oxide semiconductor (CMOS) fabrication. In particular, heterogeneous III-V silicon integration allows solutions for chip-level laser diodes and photodiodes by integrating different III-V materials into the same silicon substrate, enabling versatile functional components onto one wafer for high-level integration in varied applications (Sun J et al., 2013; Doerr, 2015; Sun C et al., 2015).

We briefly review the state-of-the-art heterogeneous III-V silicon integrated transmitting and receiving devices and the corresponding transceiving components and their characterizations, aiming for high-speed optical interconnection and high-frequency characterization.

2 Heterogeneously integrated laser diodes

2.1 Heterogeneously integrated distributed Bragg reflection (DBR) lasers

A heterogeneously integrated and CMOS compatible distributed Bragg reflection (DBR) laser diode on the back of silicon-on-insulator (SOI) chips was first proposed (Fig. 1), making CMOS-compatible interconnections and light sources on the same chip possible (Durel et al., 2016a). A single wavelength was achieved with a side-mode suppression ratio (SMSR) larger than 35 dB, and the wavelength can be tuned more than 4 nm.

‡ Corresponding author

* Project supported by the National Natural Science Foundation of China (Nos. 61875240, 61421002, and 61435010) and the Science Foundation for Youths of Sichuan Province, China (No. 2016JQ0014)

ORCID: Shang-jian ZHANG, http://orcid.org/0000-0001-9131-4002

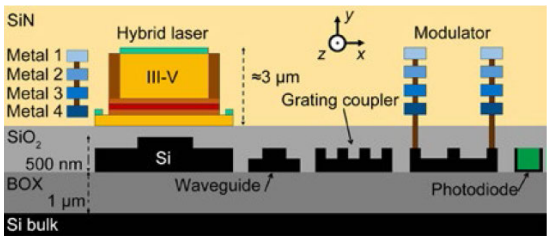

Fig. 1 Cross-section of the distributed Bragg reflection (DBR) die (Durel et al., 2016a)

Durel et al. (2016b) realized a III-V/Si laser device by the back side of SOI, and obtained a high-quality flat surface in the process at the end of the movement of non-CMOS steps. The proposed back side coupling (BSC) to solve the problem of terrain uses a new process sequence to fabricate waveguide laser alignment on the back of a silicon (Si) waveguide. A hybrid laser diode consists of an InGaAsP MQW active region (III-V epi) and a DBR cavity (Si waveguide). The same grating coupler was fabricated on the front and back of the emitter in the range of 1300–1320 nm of 1.31 μm wavelength band. Fig. 2 illustrates the coupling efficiency at two wavelengths, showing that the back configuration at 1310 nm provided an agreeable performance to that of the front configuration.

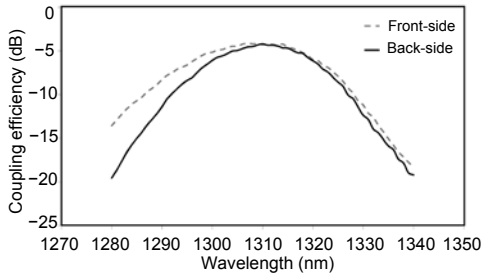

Fig. 2 Coupling efficiency at the front- and back-side wavelengths (Durel et al., 2016b)

2.2 Directly modulated distributed feedback (DFB) lasers and quantum dot (QD) lasers

A hybrid 22.5-Gb/s III-V/Si filtered distributed feedback (DFB) directly modulated laser (DML) with an enhanced dispersion tolerance (Fig. 3) operated at 1546.5 nm was proposed by Cristofori et al. (2017). Error-free transmission over 2.5-km G652 single-mode fiber was successfully demonstrated without any electronic equalization technique or dispersion compensation, showing no penalty with respect to DML back-to-back (BTB) performance.

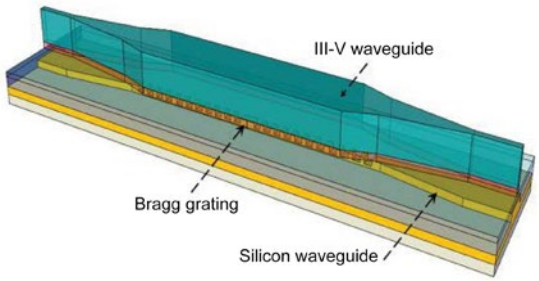

Fig. 3 Distributed feedback (DFB) laser structure (Cristofori et al., 2017)

In the case of advanced modulation, quantum dot (QD) based devices were expected to have a better performance than quantum well (QW) based devices in applications, such as mode-locked lasers and multiple wavelength lasers. Therefore, directly modulated QD laser diodes attracted a lot of attention in many uncooled environments. Then a directly modulated 1.3-μm QD laser on the Si substrate was first demonstrated by Inoue et al. (2018). A QD laser diode was 580-μm long, and showed a 6.5-GHz 3-dB bandwidth under a 116-mA bias current. Damping factor K was determined to be 0.92 ns, indicating the potential bandwidth of 9.5 GHz. Digital signal modulation with non-return-to-zero (NRZ) pattern showed a stable and open eye at a 12.5-Gb/s data rate. Fig. 4 shows the 10-Gb/t Ethernet masking test, which was in no-violation for 2027 waveforms. In the case of BTB configuration, bit error rate (BER) measurements showed error-free operation (1×10^{-13}) at a 12.5-Gb/s data rate. A 1-dB power penalty was achieved after 12-km fiber transmission.

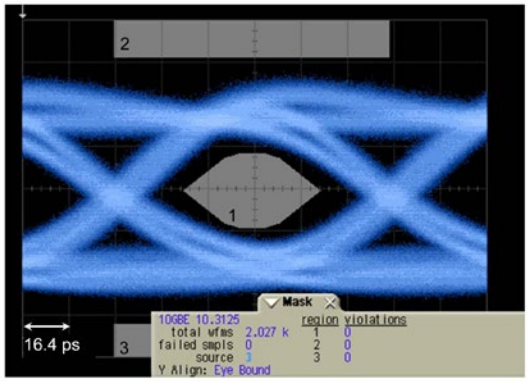

Fig. 4 Eye diagram test of the directly modulated laser (DML) (Inoue et al., 2018)

There was a single-mode QD DFB laser on the silicon substrate, demonstrated with high-temperature

(100 °C) operation and 205-A/cm^2 threshold current density. The SMSR was about 47 dB (Uvin et al., 2018).

2.3 Hybrid III-V/Si DFB lasers

A novel III-V/Si SG-DFB laser diode, which is shown in Fig. 5, was proposed by Dhoore et al. (2016). By changing only two injection currents, a laser diode can be tuned over a wavelength range larger than 55 nm. The maximum output power and SMSR obtained were over 15 dBm and 33 dB, respectively.

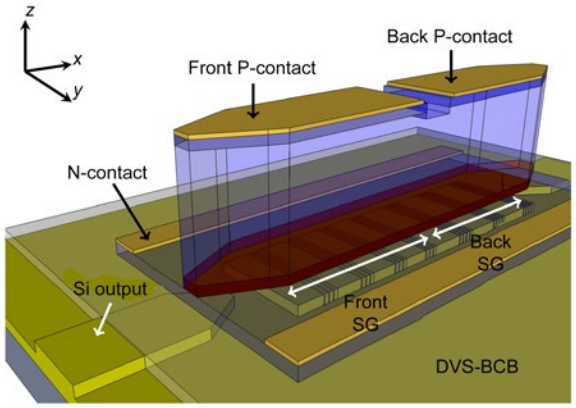

Fig. 5 Three-dimensional (3D) schematic layout of the SG-DFB laser (Dhoore et al., 2016)

A heterogeneous III-V/Si DFB laser integrated with a ring resonator was proposed by Gallet et al. (2018). The schematic structure is shown in Fig. 6. When the ring-resonator was tuned to be properly matched, an enhanced 5-dB extinction ratio could be achieved at a 25-Gb/s data rate. The DFB laser had only 2.5-dB penalty and 20-dB power budget for 20-km single-mode fiber transmission.

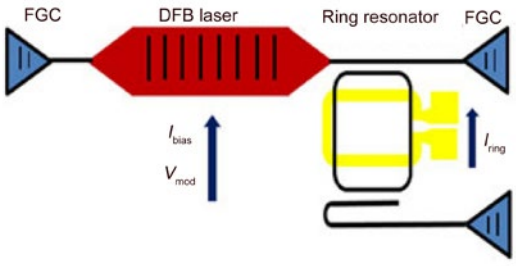

Fig. 6 Hybrid III-V/Si CML laser diode (Gallet et al., 2018)

A heterogeneously integrated DFB was demonstrated with an active region layer by transferring the 40×970 μm^2 III-V epitaxial on Si (Zhang et al., 2018). Mode selection cavity was realized with a second-order grating defined in the silicon layer with a 477-nm period and 75% duty cycle. The DFB laser diode has a 18-mA threshold current and above 2-mW maximum output power at 20 °C. In the about 1550-nm single-mode operation, SMSR was achieved with larger than 40 dB.

2.4 Hybrid III-V/Si Fabry-Perot (FP) lasers

The hybrid III-V/Si Fabry-Perot (FP) laser diode with a metal-coated etching mirror was proposed by Lee et al. (2016). Generic integrated FP laser diodes were realized in the way of a SiO_2 interlayer wafer bonding under a low temperature (Fig. 7). Compared with the conventional direct wafer bonding, interlayer wafer bonding was simpler and had lower risk. Laser diodes with this design achieve a laser threshold of about 50 mA and output power of about 9 mW.

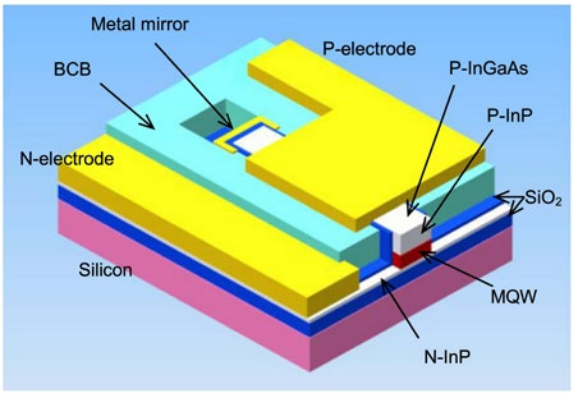

Fig. 7 III-V/Si Fabry-Perot (FP) laser diode (Lee et al., 2016)

2.5 Quantum-well lasers grown on Si

InGaAs/InAlGaAs multi-quantum-well (MQW) lasers directly grown on on-axis V-grooved (001) Si by metalorganic chemical vapor deposition (MOCVD) was first introduced by Zhu et al. (2018). The structure is shown in Fig. 8. Laser wavelength at around 1550 nm was observed under a threshold current density J_{th}=3.3 kA/cm^2 at pulsed current injection at room temperature. Characteristic temperature T_0 was measured about 133 K in the range of 20–40 °C. Large-area InP on Si substrates had potential for applications, such as different III-V/Si lasers, photodiodes, and transistors.

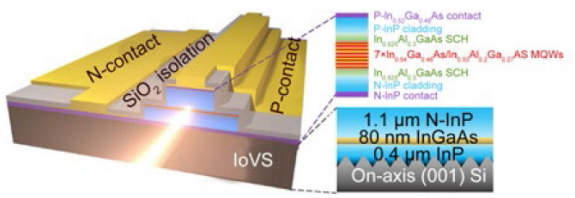

Fig. 8 Quantum-well laser diode grown on silicon (Zhu et al., 2018)

2.6 Widely tunable lasers

An external cavity laser with III-V/Si integration that could be tuned within a wavelength range up to 60 nm at the 1550-nm band was proposed by Guan et al. (2018). The III-V semiconductor gain chip was mixed and coupled into silicon chip through a Si_3N_4 spot size converter. This type of laser diode was suitable for high-volume production, because only passive alignment was required in packaging. The maximum output power of this laser was 11 mW, and the wavelength range was 60 nm around the 1550-nm band with typical SMSR of larger than 46 dB. The linewidth was larger than 80 kHz across the 1550-nm band. The smallest linewidth of 37 kHz was the best performance with a silicon-based external cavity. In an experiment, Guan et al. (2018) showed a complete optical link with >250 Gb/s coherent transmission.

The external cavity laser adopted a ring structure to improve the lasing performance, such as SMSR, linewidth, and frequency chirp. Therefore, the laser can be designed and fabricated with more than one ring, with which the tuning range can be remarkably extended by the Vernier effect. Heterogeneously integrated ring-based Vernier lasers had a 330-kHz linewidth (Hulme et al., 2013). Improved design with coupled-ring-resonator (CRR) lasers had an even larger linewidth of 160 kHz (Komljenovic et al., 2015a; Srinivasan et al., 2015). Threshold currents were around 50 mA, while output powers were larger than 15 mW. The CRR-based lasers had the advantage of a descending-port bus waveguide to form the necessary filter shape and a simple dual-output-port laser with a higher external differential quantum efficiency.

Further progress was achieved using a heterogeneously integrated external cavity (Komljenovic et al., 2015b) with a 4-cm long low-loss waveguide. The measured linewidth in the full tuning range was smaller than 100 kHz, while the best results were around 50 kHz. The threshold current was about 30 mA, when the output power was larger than 10 mW. In the whole tuning range, SMSR was larger than 45 dB.

In addition, we made a detailed performance comparison for recent works on the heterogeneously integrated laser diodes (Table 1).

3 Integrated III-V/Si photodiodes

The heterogeneous hybrid III-V/Si platform enables the inclusion of optical active devices in a photonic integration circuit flexible. The III-V active layer was usually bonded to the silicon-on-insulator (SOI) waveguide, or epitaxially grown on Si (Liu et al., 2014).

Beling et al. (2013) demonstrated III-V/Si photonic components with silicon nitride waveguides for novel photonic integration circuits. InGaAs photodiodes (PDs) in PIC had an average fiber coupled 0.36-A/W responsivity at the 1550-nm band and a 30-GHz electrical bandwidth. The hybrid III-V/Si devices integrated with Si_3N_4 waveguides are shown in Fig. 9.

Table 1 Performance comparison of different integrated laser diodes

Type of laser	SMSR (dB)	λ-tunability (nm)	λ (nm)	I (mA)	Power (mW)
Heterogeneously integrated DBR lasers (Durel et al., 2016a)	35	4	–	–	–
Directly modulated DFB lasers (Cristofori et al., 2017)	40	–	1546.5	–	–
Single-mode QD DFB lasers on silicon (Uvin et al., 2018)	47	–	1300.0	9.5	–
Hybrid III-V/Si DFB lasers (Dhoore et al., 2016)	33	55		–	31.6
Heterogeneously integrated DFB lasers (Zhang et al., 2018)	40		1550.0	18.0	–
Hybrid III-V/Si FP lasers (Lee et al., 2016)			1575.0	50.0	9.0
External cavity lasers with III-V/Si integration (Guan et al., 2018)	46	60	1550.0	–	11.0
Coupled-ring-resonator (CRR) lasers (Komljenovic et al., 2015b; Srinivasan et al., 2015)	–	–	–	50.0	<15.0

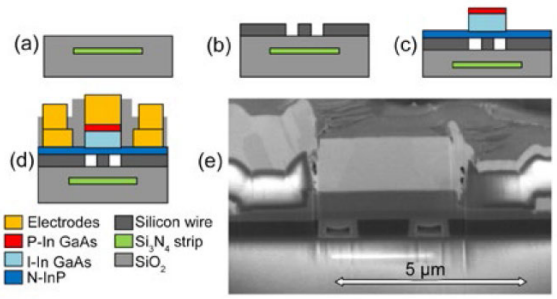

Fig. 9 Process flow and cross-section of hybrid III-V/Si optoelectronic devices integrated with Si_3N_4 waveguides: (a) Si_3N_4 waveguide after fabrication in a CMOS foundry; (b) Si_3N_4 waveguide with patterned silicon waveguides; (c) III-V epitaxial layers bonded to silicon and partially completed; (d) III-V/Si PDs; (e) underlying Si_3N_4 waveguide (Piels et al., 2014)

Uni-traveling carrier (UTC) designs are efficient in improving the bandwidth and output power of III-V/Si PDs. Fig. 10 shows a UTC PD (Beling et al., 2013). Internal responsivities were 0.85 A/W, and the operating bandwidth was 30 GHz. The maximum radio frequency (RF) output power was 3.9 dBm at 30 GHz, while it reached 5.6 dBm at 20 GHz.

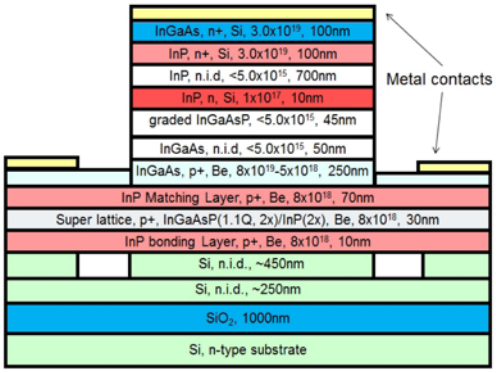

Fig. 10 Hybrid III-V/Si UTC PD (Beling et al., 2013)

PDs with low dark currents were successfully realized based on III-V materials grown on a Si substrate (Sun et al., 2018). Dark currents were as low as 10 nA at the 3-V reverse bias, while the responsivities were as high as 0.79 A/W. PDs with a positive-intrinsic-negative (PIN) structure achieved a 7-GHz bandwidth, while those with a modified uni-traveling carrier (MUTC) structure achieved a 9-GHz bandwidth. The RF saturation power reached 2.6 dBm, and the OIP_3 was kept larger than 15 dBm. Figs. 11a and 11b show the low dark current and the micrograph of PD, respectively.

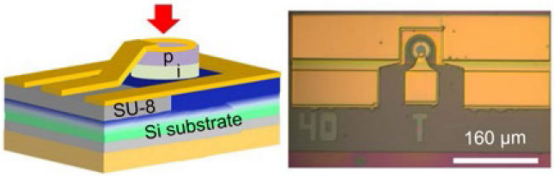

Fig. 11 Low dark current (a) and micrograph (b) of PD (Sun et al., 2018)

4 Integrated network-on-chip (NoC)

An optical network-on-chip (NoC) enables data flow among transceiver nodes in the photonic integration circuit architecture high capacity. There were many optical NoCs (Ye et al., 2013; Le Beux et al., 2014), such as Corona (Vantrease et al., 2008), Firefly (Pan et al., 2009), and ATAC (Kurian et al., 2010), with two- or three-dimensional photonic integration techniques.

Corona's NoC is based on a microring resonator structure with a common bus waveguide, and different microring resonators are operated at different wavelength divison multiplexing (WDM) channels to realize electro-optic modulation/multiplexing or optoelectronic demultiplexing and photodetection.

Zhang et al. (2016) reported an optical NoC architecture (Fig. 12). Transceiver nodes were connected to a common bus waveguide through broadband optical switches. Every transceiver node had its own interface with a CMOS driver from electrical to optical conversion or from optical to electrical conversion. NoC could be operated and configured at a different status by setting the broadband optical switches. In the default status, the transmitter was directly connected to its local receiver for self-communication or self-initialization (Fig. 12a). By fully setting two different switches in the bus waveguide, two different nodes could be connected through one transmitter in this node to one receiver in another node for point-to-point communication (Fig. 12b). Network could be operated at broadcast communication for one transmitter in one node to other receivers in the rest of nodes by partially setting the other switches in the bus waveguide (Fig. 12b). The NoC architecture brought a lot of configurability and flexibility in practical system applications.

Inside the NoC, there were eight WDM channels in the 1550-nm band with a 1.6-nm wavelength

spacing (International Telecommunications Union grid). The transmitter in every wavelength channel consists of a DFB laser as the continuous-wave (CW) optical source, a high-frequency electroabsorption modulator (EAM) for electro-optic modulation, and a monitoring PD (MPD) for in-situ power monitoring. The corresponding receiver includes high-speed PIN PDs (FPDs) with an InGaAs absorptive layer bonded on silicon. SOAs before the photodiodes were used to boost the received optical power to compensate for link loss. The eight-channel array waveguide gratings (AWGs) were fabricated in silicon and adopted as channel MUX/DEMUX in the optical domain.

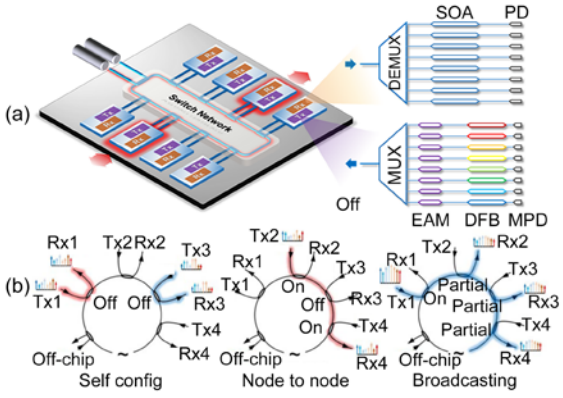

Fig. 12 Heterogeneously integrated NoC: (a) architecture; (b) reconfiguration

Most elements in the NoC could be fabricated on heterogeneous silicon or on the III-V/Si integration platform, including DFB laser diodes, high-frequency Mach-Zehnder or EAM modulators (MZMs or EAMs), and high-speed PDs (Zhang et al., 2017). Fabrication of the NoC circuit was categorized as a pure silicon process for passive and III-V/Si processes for the most active devices. Silicon process was used to fabricate waveguide, waveguide grating, wavelength multiplexer, demultiplexer, etc., on the SOI substrate with a buried oxide (BOX) layer. III-V epitaxial layer structures were separately fabricated and then bonded to the appropriate devices.

Fig. 13 shows a stitching microscope image of the photonic NoC after III-V/Si bonding. The whole die was about 19 mm×19 mm. Transceiver circuits were located in the middle of the die with a size of about 11 mm×16 mm. There were over 400 functional photonic components in the NoC. The footprint of each transceiver node was about 1 mm×6 mm, which was limited mainly by the size of the AWGs. The switch array was located at the right side of the chip with metal pads for setting work status.

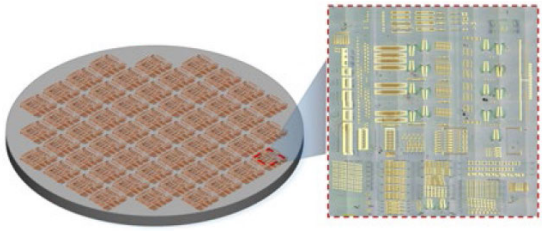

Fig. 13 Microscope image of a photonic NoC

5 Integrated on-chip characterization

Fig. 14 shows the experimental setup for on-chip communication with an NoC network. The switch array was controlled by a 16-pin probe card to set the work status of the switch array. The EAM modulator and photodiode were driven by two ground-signal-ground (GSG) microwave probes for a high-speed RF signal connection, and high-speed bias-tees to provide DC reverse voltage bias on the EAM and PD. Wideband microwave amplifiers were used to boost the driving RF signal to the EAM modulator and the receiving RF signal from the PD. The NoC retained edge waveguide taper for the optional external input/output (I/O).

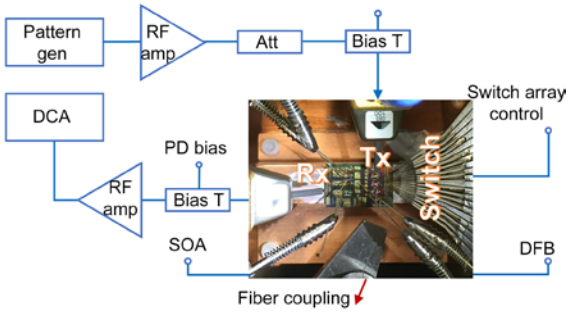

Fig. 14 Experimental setup for NoC communication

Small-signal frequency response of the transmitter-receiver link was swept by a network vector analyzer and characterized as a 24 GHz 6-dB bandwidth (Fig. 15). A digital modulation signal was applied to the EAM modulator through a 40-Gb/s pattern generator and a (2^7-1) pseudo random bit sequence (PRBS) pattern. Eye diagrams at 28, 30, 35, and 40 Gb/s data rates are shown in Fig. 16. Transmission performance showed the potential capacity of

320 Gb/s (8×40 Gb/s) per transceiver (node) and 2.56 Tb/s (8×320 Gb/s) for an NoC network.

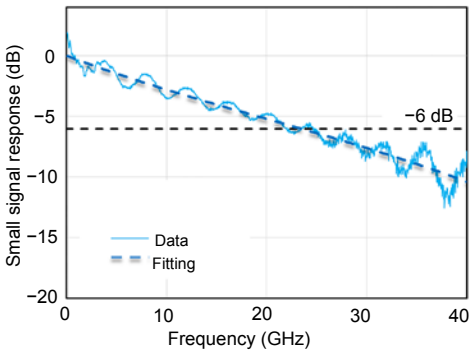

Fig. 15 Frequency response of transmitter-receiver link

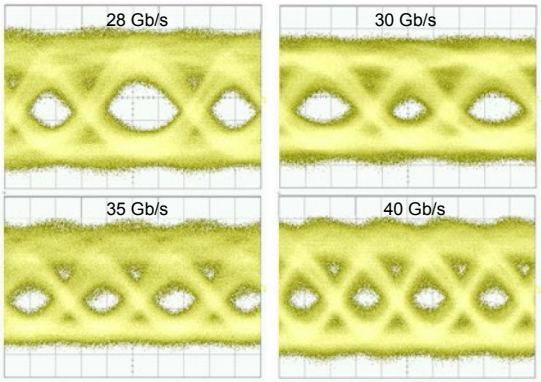

Fig. 16 Eye diagrams of digital communication of NoC

For on-chip characterization of EAMs and PDs, we used a heterodyne test, where the laser diode (LD) and EAM were probed with radio-frequency microwave signals $v_0(t)=V_0\cos(2\pi f_0 t+\varphi_0)$ and $v_1(t)=V_1\cos(2\pi f_1 t+\varphi_1)$, respectively, and the received optical signal was detected by PDs for photodetection, which can be expressed in the time domain as

$$i_r(t)=RP_0\left[1+m_0(f_0)\cos(2\pi f_0 t+\varphi_0)\right]\cdot\left[1+m_1(f_1)\cos(2\pi f_1 t+\varphi_1)\right], \quad (1)$$

where P_0 is the optical power of LD, m_0 the modulation index of LD, m_1 the modulation index of EAM, and R the responsivity of PD. From Eq. (1), we can quantify the recovered electrical signal at the desired frequency as

$$i_r(f_0)=P_0R(f_0)m_0(f_0), \quad (2)$$

$$i_r(f_0\pm f_1)=0.5P_0R(f_0\pm f_1)m_0(f_0)m_1(f_1). \quad (3)$$

In the EAM test, frequencies of two RF signals were set as $f_1\approx 2f_0$, so that $R(f_0)\approx R(f_1-f_0)$ can be held. In this case, the modulation index can be subtracted from the output electrical heterodyne signals based on Eqs. (2) and (3), expressed as

$$m_1(f_1)=2i_r(f_1-f_0)/i_r(f_0), \quad f_1\approx 2f. \quad (4)$$

For example, two RF driving signals were chosen as $f_1=2f_0+0.004$ GHz, while the recovered electrical signal from a PD was collected and analyzed at the frequencies of f_0 and f_1-f_0. Figs. 17a and 17b illustrate the measured conversion loss from input frequency f_1 to output frequencies f_0 and f_1-f_0. Therefore, the modulation index of EAM can be determined (Fig. 17c). Measurement can be repeated at other driving frequencies, and the frequency response of EAM under the same driving level can be plotted as a function of modulation frequency (Fig. 17c).

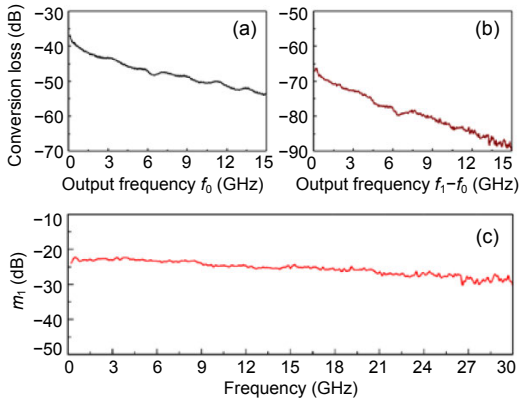

Fig. 17 On-chip EAM characterization from conversion loss at the frequencies of f_0 (a) and f_1-f_0 (b), and measured frequency response of EAM under the same driving level (c)

In the PD test, two RF signals were set as $f_0\approx f_1$, kept at the lowest fixed frequency f_0-f_1, and close to DC, so that recovered electrical signals at the sum-and-difference frequencies $f_0\pm f_1$ were analyzed. PD responsivity can be determined by the relative amplitudes at f_0+f_1 and at f_0-f_1, as follows:

$$R(f)=\frac{R(f_0+f_1)}{R(f_0-f_1)}=\frac{i_r(f_0+f_1)}{i_r(f_0-f_1)}. \quad (5)$$

From Eq. (3), the sum-and-difference frequency components had the same terms of $m_1(f)$ and $m_0(f)$, so

the measurement of PD responsivity eliminated the influence of the EAM, i.e., a self-calibrated measurement of PD. For example, two RF signals were chosen as $f_0=f_1+0.1$ GHz, while the recovered electrical signal from the PD was analyzed at the desired sum-and-difference frequencies $f_0\pm f_1$. Figs. 18a and 18b show the conversion loss at the sum-and-difference frequencies, from which the frequency response of the PD can be subtracted and illustrated as a function of frequency (Fig. 18c).

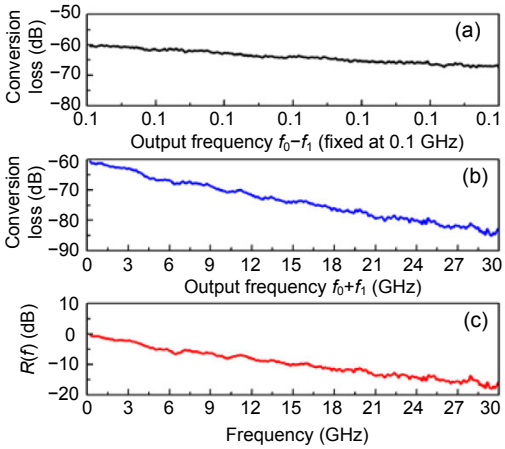

Fig. 18 PD characterization from conversion loss at the frequencies of f_0-f_1 (a) and f_0+f_1 (b), and the measured frequency response of PD (c)

6 Conclusions

We have reviewed the recent heterogeneous III-V/Si photonics integrated devices and components. We believe that the heterogeneous III-V on silicon is promising for ultra-dense photonic integration for future high-speed data transmission.

Acknowledgements

We thank Chong ZHANG, Jon PETERS, and John BOWERS from University of California, Santa Barbara (UCSB) for their cooperation and help.

References

Arakawa Y, Nakamura T, Urino Y, et al., 2013. Silicon photonics for next generation system integration platform. *IEEE Commun Mag*, 51(3):72-77. https://doi.org/10.1109/MCOM.2013.6476868

Beling A, Cross AS, Piels M, et al., 2013. InP-based waveguide photodiodes heterogeneously integrated on silicon-on-insulator for photonic microwave generation. *Opt Expr*, 21(22):25901-25906. https://doi.org/10.1364/OE.21.025901

Cristofori V, da Ros F, Ozolins O, et al., 2017. 25-Gb/s transmission over 2.5-km SSMF by silicon MRR enhanced 1.55-μm III-V/SOI DML. *IEEE Photon Technol Lett*, 29(12):960-963. https://doi.org/ 10.1109/LPT.2017.2700497

Dhoore S, Li LY, Abbasi A, et al., 2016. Demonstration of a discretely tunable III-V-on-silicon sampled grating DFB laser. *IEEE Photon Technol Lett*, 28(21):2343-2346. https://doi.org/10.1109/LPT.2016.2593983

Doerr C, 2015. Silicon photonic integration in telecommunications. *Front Phys*, 3(2):137-179. https://doi.org/10.3389/fphy.2015.00037

Durel J, Bakir BB, Jany C, et al., 2016a. First demonstration of a back-side integrated heterogeneous hybrid III-V/Si DBR lasers for Si-photonics applications. IEEE Int Electron Devices Meeting, p.584-587. https://doi.org/10.1109/IEDM.2016.7838471

Durel J, Ferrotti T, Chantre A, et al., 2016b. Realization of back-side heterogeneous hybrid III-V/Si DBR lasers for silicon photonics. Proc SPIE, p.1-12. https://doi.org/10.1117/12.2212309

Gallet A, Levaufre G, Accard A, et al., 2018. Hybrid III-V on silicon integrated distributed feedback laser and ring resonator for 25 Gb/s future access networks. *J Lightw Technol*, 36(8):1498-1502. https://doi.org/10.1109/JLT.2017.2782012

Guan H, Novack A, Galfsky T, et al., 2018. Widely-tunable, narrow-linewidth III-V/silicon hybrid external-cavity laser for coherent communication. *Opt Expr*, 26(7): 7920-7933. https://doi.org/10.1364/OE.26.007920

Hulme JC, Doylend JK, Bowers JE, 2013. Widely tunable vernier ring laser on heterogeneous silicon. *Opt Expr*, 21(17):19718-19722. https://doi.org/10.1364/OE.21.019718

Inoue D, Jung D, Norman J, et al., 2018. Directly modulated 1.3 μm quantum dot lasers epitaxially grown on silicon. *Opt Expr*, 26(6):7022-7033. https://doi.org/10.1364/OE.26.007022

Komljenovic T, Davenport M, Srinivasan S, et al., 2015a. Narrow linewidth tunable laser using coupled resonator mirrors. Optical Fiber Communications Conf, p.1-3. https://doi.org/10.1364/OFC.2015.W2A.52

Komljenovic T, Srinivasan S, Norberg E, et al., 2015b. Widely tunable narrow-linewidth monolithically integrated external-cavity semiconductor lasers. *IEEE J Sel Top Quant Electr*, 21(6):1501909. https://doi.org/10.1109/JSTQE.2015.2422752

Kurian G, Miller JE, Psota J, et al., 2010. ATAC: a 1000-core cache-coherent processor with on-chip optical network. 19th Int Conf on Parallel Architectures and Compilation Techniques, p.477-488. https://doi.org/10.1145/1854273.1854332

Le Beux S, Li H, O'Connor I, et al., 2014. Chameleon: channel efficient optical network-on-chip. Proc Design,

Automation & Test in Europe Conf & Exhibition, p.1-6. https://doi.org/10.7873/DATE.2014.317

Lee CW, Ng DKT, Ren M, et al., 2016. Generic heterogeneously integrated III–V lasers-on-chip with metal-coated etched-mirror. *IEEE J Sel Top Quant Electr*, 22(6): 1500409. https://doi.org/10.1109/JSTQE.2016.2549800

Liu AY, Zhang C, Norman J, et al., 2014. High performance continuous wave 1.3 μm quantum dot lasers on silicon. *Appl Phys Lett*, 104(4):041104. https://doi.org/10.1063/1.4863223

Pan Y, Kumar P, Kim J, et al., 2009. Firefly: illuminating future network-on-chip with nanophotonics. Int Symp on Computer Architecture, p.429-440. https://doi.org/10.1145/1555754.1555808

Piels M, Bauters JF, Davenport ML, et al, 2014. Low-loss silicon nitride AWG demultiplexer heterogeneously integrated with hybrid III–V/silicon photodetectors. *J Lightw Technol*, 32(4):817-823.

Srinivasan S, Davenport M, Komljenovic T, et al., 2015. Coupled-ring-resonator-mirror-based heterogeneous III-V silicon tunable laser. *IEEE Photon J*, 7(3):2700908. https://doi.org/10.1109/JPHOT.2015.2428255

Sun C, Wade MT, Lee Y, et al., 2015. Single-chip microprocessor that communicates directly using light. *Nature*, 528(7583):534-538. https://doi.org/10.1038/nature16454

Sun J, Timurdogan E, Yaacobi A, et al., 2013. Large-scale nanophotonic phased array. *Nature*, 493(7431):195-199. https://doi.org/10.1038/nature11727

Sun KY, Jung D, Shang C, et al., 2018. Low dark current III-V on silicon photodiodes by heteroepitaxy. *Opt Expr*, 26(10):13605-13613. https://doi.org/10.1364/OE.26.013605

Uvin S, Kumari S, de Groote A, et al., 2018. 1.3 μm InAs/GaAs quantum dot DFB laser integrated on a Si waveguide circuit by means of adhesive die-to-wafer bonding. *Opt Expr*, 26(14):18302-18309. https://doi.org/10.1364/OE.26.018302

Vantrease D, Schreiber R, Monchiero M, et al., 2008. Corona: system implications of emerging nanophotonic technology. 35th Int Symp on Computer Architecture, p.153-164. https://doi.org/10.1109/ISCA.2008.35

Ye YY, Xu J, Huang BH, et al., 2013. 3-D mesh-based optical network-on-chip for multiprocessor system-on-chip. *IEEE Trans Comput Aid Des Int*, 32(4):584-596. https://doi.org/10.1109/TCAD.2012.2228739

Zhang C, Zhang SJ, Peters JD, et al., 2016. 2.56 Tbps (8×8×40 Gbps) fully-integrated silicon photonic interconnection circuit. Conf on Lasers and Electro-Optics, p.1-2. https://doi.org/10.1364/CLEO_AT.2016.JTh4C.4

Zhang J, Haq B, O'Callaghan J, et al., 2018. Transfer-printing-based integration of a III-V-on-silicon distributed feedback laser. *Opt Expr*, 26(7):8821-8830. https://doi.org/10.1364/OE.26.008821

Zhang SJ, Zhang C, Wang H, et al., 2017. On-wafer probing-kit for RF characterization of silicon photonic integrated transceivers. *Opt Expr*, 25(12):13340-13350. https://doi.org/10.1364/oe.25.013340

Zhu S, Shi B, Li Q, et al., 2018. Room-temperature electrically-pumped 1.5μm InGaAs/InAlGaAs laser monolithically grown on on-axis (001) Si. *Opt Expr*, 26(11):14514-14523. https://doi.org/10.1364/OE.26.014514